Draft version May 27, 2008
Preprint typeset using LaTeX style emulateapj v. 03/07/07

DUST EMISSION FROM THE PERSEUS MOLECULAR CLOUD

S. Schnee[1], J. Li[2], A. A. Goodman[2] & A. I. Sargent[1]

Draft version May 27, 2008

ABSTRACT

Using far-infrared emission maps taken by IRAS and Spitzer and a near-infrared extinction map derived from 2MASS data, we have made dust temperature and column density maps of the Perseus molecular cloud. We show that the emission from transiently heated very small grains and the big grain dust emissivity vary as a function of extinction and dust temperature, with higher dust emissivities for colder grains. This variable emissivity can not be explained by temperature gradients along the line of sight or by noise in the emission maps, but is consistent with grain growth in the higher density and lower temperature regions. By accounting for the variations in the dust emissivity and VSG emission, we are able to map the temperature and column density of a nearby molecular cloud with better accuracy than has previously been possible.

Subject headings: ISM: clouds — dust, extinction — surveys

1. INTRODUCTION

Far-infrared and sub-millimeter continuum radiation from interstellar clouds is typically attributed mostly to "dust." In truth, however, even the contributions from "dust" come from multiple populations of grain types, which are each at a mixture of temperatures. Along any given line of sight, there may be random or systematic variations both in the admixture of grain types and in their temperature, and those variations may or may not be correlated. Historically, researchers have used more and more complicated procedures to account for dust emission and estimate column density.

The simplest way to infer column density from "thermal" dust emission is to assume a single grain type, radiating with a single efficiency (opacity), at a single temperature. In that case, flux at any wavelength can be converted to a column density, assuming a dust temperature. The next-most-sophisticated approach is to use observations at two wavelengths, and to infer a color temperature, by assuming that the dust emission comes from a modified blackbody, which has a wavelength-dependent emissivity one takes as given (e.g., Wood et al. 1994).

With observations at three wavelengths, it should be possible to also constrain the dust emissivity, assuming its functional dependence on wavelength is known and is described by just one parameter ($\kappa_\lambda \propto \lambda^{-\beta}$). As Schnee et al. (2007) have shown, however, a three-wavelength constraint on T_d, N_d and β independently is only possible for the case of very (to date unrealistically) high signal-to-noise data. Nevertheless, with three wavelengths of very high S/N, or measurements at four or more wavelengths, one could constrain the temperature, column density and emissivity independently – if only all the mixtures of grains along lines of sight were similar, and the temperature distribution along the line of sight were isothermal.

In an earlier paper, (Schnee et al. 2006, hereafter SBG), we showed that line-of-sight variations in the dust temperature account for nearly all the scatter in a plot of dust-emission vs. dust-extinction derived column density in the Perseus molecular cloud. In Schnee et al. (2005, hereafter SRGL), we found that Very Small Grains (VSG's) are likely to account for a large fraction ($> 50\%$) of the dust emission at wavelengths shorter that 100 μm. If that fraction is relatively constant, then one can say that Big Grains (BG's) are a good proxy for column density, modulo the uncertainty imposed by the line-of-sight variations in the dust temperature. However, if the VSG contribution is not constant, but depends on either N_d or T_d, then the situation is further confounded. In this paper, we explore all of these possibilities, and we find, in agreement with earlier works (e.g., Stepnik et al. 2003), that the VSG contribution does seem to vary systematically with T_d and N_d, and that it is important to account for this effect in estimates of dust column density and dust temperature.

2. OBSERVATIONS

SRGL showed that far-infrared emission maps can be used to determine the dust temperature and column density in molecular clouds once the conversion between FIR optical depth and V-band extinction has been determined. This analysis took advantage of the IRIS (Improved Reprocessing of the IRAS Survey) maps at 60 and 100 μm (Miville-Deschênes & Lagache 2005) and near-infrared extinction map created from 2MASS data as part of the COMPLETE (COordinated Molecular Probe Line Extinction and Thermal Emission) Survey of Star Forming Regions (Ridge et al. 2006). Subsequently, SBG demonstrated that the column density determined from pairs of FIR emission maps should become more accurate and less biased when the emission is measured at longer wavelengths due to the decreased influence of line-of-sight temperature variations.

With the recent release of 70 and 160 μm maps of Perseus taken with the Spitzer Space Telescope (Evans et al. 2003; Rebull et al. 2007), we can improve upon the SRGL analysis. In this short paper, we combine the 100 μm IRIS and 160 μm Spitzer maps to derive dust temperature and column density maps that are not strongly

Electronic address: schnee@astro.caltech.edu
[1] Division of Physics, Mathematics and Astronomy, California Institute of Technology, 770 South Wilson Avenue, Pasadena, CA 91125
[2] Harvard-Smithsonian Center for Astrophysics, 60 Garden Street, Cambridge, MA 02138

biased by the emission from transiently heated VSG's. In addition we are able to estimate the variation of the VSG emission and BG emissivity with T_d and A_V.

2.1. *Spitzer*

We used the 70 and 160 μm emission maps of the Perseus molecular cloud from the Spitzer Science Archive that were taken as part of the Spitzer Legacy Program "From Molecular Cores to Planet-forming Disks" (c2d) (Evans et al. 2003; Rebull et al. 2007). Map resolutions are $18''$ and $40''$ at 70 and 160 μm, respectively. The c2d delivery includes error maps, which account for systematic and random errors. The overall gain calibration uncertainty is $\sim$5% at 70 μm (Gordon et al. 2007) and $\sim$12% at 160 μm (Stansberry et al. 2007). The c2d error maps show that the random error for maps smoothed to $5'$ resolution (the resolution of the extinction map) is $<$1% at both 70 and 160 μm.

We applied color corrections to these archival fluxes since they were determined assuming that the emission is from a blackbody at 10,000 K while we have assumed that the emission comes from a modified blackbody with emissivity spectral index $\beta = 2$ (Draine & Lee 1984) and equilibrium temperature to be determined, but certainly less than 10,000 K (Schlegel et al. 1998). The color correction, which is combined with the dust temperature calculation, is futher described in Sect. 3.1.

2.2. *IRAS/IRIS*

IRIS flux density maps at 60 and 100 μm, in contrast with earlier releases of the IRAS all-sky maps, have been corrected for the effects of zodiacal dust and striping, and have the proper gain and offset calibration (Miville-Deschênes & Lagache 2005). The IRIS maps of Perseus have a resolution of approximately $4\farcm3$ (though we smooth them to the $5'$ resolution of our NIR extinction map for all analyses). The noise in the IRAS maps is approximately 0.03 MJy sr^{-1} and 0.06 MJy sr^{-1} at 60 and 100 μm (Miville-Deschênes & Lagache 2005), which is $\lesssim$1% of the flux in the portion of Perseus included in the c2d survey. Like the Spitzer maps, these were color-corrected by us (following the IRAS Explanatory Supplement VI C.3). For consistency, we consider only the region of Perseus covered by the c2d MIPS maps at 70 and 160 μm in this analysis.

2.3. *NIR Extinction Map*

An extinction map of Perseus based on the Two Micron All Sky Survey (2MASS) point source catalog was created as part of the COMPLETE survey (Ridge et al. 2006) using the NICER algorithm, devised by Lombardi & Alves (2001). This algorithm uses the near-infrared color excess of background stars to estimate the column density of foreground dust. When directly comparing NIR and FIR-derived column densities (e.g., Figs. 2, 4 and 9), all maps have been smoothed to a common resolution of $5'$, since that is the resolution of the NICER extinction map of Perseus.

3. ANALYSIS

The flux density emitted by dust in thermal equilibrium is given by

$$S_\nu = \Omega B_\nu(T_d) N_d \alpha \nu^\beta, \quad (1)$$

where

$$B_\nu(T_d) = \frac{2h\nu^3}{c^2} \frac{1}{\exp(h\nu/kT_d) - 1} \quad (2)$$

In Equation 1, S_ν is the observed flux density at frequency ν; Ω is the solid angle of the beam; $B_\nu(T_d)$ is the blackbody emission from the dust at temperature T_d; N_d is the column density of dust, α is a constant that relates the flux density to the optical depth of the dust at frequency ν, and β is the emissivity spectral index of the dust, which we assume to be 2 throughout this paper (Draine & Lee 1984). In SRGL we showed that $\beta = 2$ is a reasonable value for the cold dust in Perseus.

Equation 1 is only true for BG's in thermal equilibrium, and does not describe the emission from stochastically heated VSG's, which cannot be characterized by an equilibrium temperature (Draine & Li 2001). The VSG's are expected to be a significant component of the observed emission in the IRAS 60 μm and Spitzer 70 μm bands, but are not expected to contribute much in the IRAS 100 μm and Spitzer 160 μm bands (Li & Draine 2001). If we were to ignore the VSG emission, we would systematically overestimate the dust temperature and underestimate the column density in Perseus. We therefore account for it using a procedure that improves upon that adopted by SRGL, as described below.

3.1. *Dust Temperature*

The fluxes quoted in the IRAS and Spitzer emission maps are derived from the total energy detected convolved with the wavelength-dependent instrumental response and an assumed SED of the emitting source. The quoted flux density at wavelength λ_0 is related to the intrinsic flux density by:

$$F_{\lambda_0}^{quoted} = \frac{\int (F_\lambda^{intrinsic}/F_{\lambda_0}^{intrinsic}) \lambda R_\lambda d\lambda}{\int (F_\lambda^{default}/F_{\lambda_0}^{default}) \lambda R_\lambda d\lambda} F_{\lambda_0}^{intrinsic} \quad (3)$$

(Stansberry et al. 2007) where $F_\lambda^{intrinsic}$ is the true source SED, $F_\lambda^{default}$ is the default SED and R_λ is the instrumental response function (the sensivity of the detector as a function of wavelength). The default SED for the Spitzer data is that of a 10,000 K blackbody, while the default SED for the IRIS data is $F_\lambda \propto 1/\lambda$. We assume that the intrinsic SED is a modified blackbody with $\beta = 2$ (Draine & Lee 1984), so the color correction is temperature dependent.

To derive the color correction and dust temperature, we create a lookup table of the intrinsic flux density at λ = 60, 70, 100 and 160 μm for dust at temperatures between 5 and 100 K, at 0.1 K intervals. We then calculate what flux density would have been quoted at those wavelengths using Eq. 3. Using this table, we are able to derive the color-corrected dust temperature from the ratio of the *quoted* flux densities, making the assumption that the dust emission is optically thin and isothermal along each line of sight. The IRAS 100 μm and Spitzer 160 μm maps are not significantly corrupted by VSG emission, so we derive a dust temperature map using our lookup table and the quoted F_{100}/F_{160} after smoothing the emission maps to a common ($5'$) resolution.

The IRAS 60 and Spitzer 70 μm flux densities come from a combination of BG and VSG emission, but Equations 1 and 3 are only accurate for BG emission. In SRGL

we removed the VSG emission by assuming that a constant fraction of all 60 μm emission can be attributed to VSG's. This proportion was found by minimizing the difference between the temperature maps derived from IRIS data and the dust temperature map derived by Schlegel et al. (1998), which was derived from DIRBE 100 and 240 μm emission (and therefore free from VSG contamination).

However, the proportion of 60 and 70 μm flux emitted by VSG's is expected to vary with environment. In regions with high extinction, the VSG's will be shielded from the ISRF and will therefore not be effectively heated. In cold, dense regions dust grains may stick together, removing the VSG population. For instance, Stepnik et al. (2003) have shown that the VSG emission is greatly reduced in a dense filament in Taurus where $A_V > 2.1$ and found a corresponding increase in the dust emissivity. A similar transition region of altered dust composition has been reported using IRAS 60 and 100 μm emission maps (e.g., Laureijs et al. 1991, 1989; Boulanger et al. 1990).

Here we take advantage of the higher resolution of the IRAS 100 and Spizter 160 μm images, as compared with the DIRBE maps, to remove the emission from VSG's accounting for spatial variations in their contribution. We divide our 100/160 μm derived temperature maps into ten equally populated temperature and extinction subsets (five temperature subsets for A_V less than the median NIR-derived extinction and five temperature subsets for higher A_V) and calculate the VSG contribution to the 60 and 70 μm emission independently for each bin using the dust temperature derived from the 100/160 μm pair of emission maps. In each bin, we multiply the 60 and 70 μm emission (smoothed to 5′ resolution) by the scaling factors f_{60} and f_{70} which are chosen such that the temperatures derived from $f_{60}F_{60}/F_{100}$ and $f_{70}F_{70}/F_{160}$ are best matched to the dust temperature derived from F_{100}/F_{160}. The comparatively low resolution of the DIRBE-derived temperature map prevented us from performing this more sophisticated correction in SRGL. The scale factors (f_{60} and f_{70}) used to account for the VSG emission are shown in Fig. 1. Our assumptions that dust is isothermal along each line of sight and that the dust emissivity (characterized by α and β in Eq. 1) is constant introduce uncertainties into our calculations. The effect of assuming isothermality is covered in SBG, and we discuss the effects of variable dust emissivity in Section 3.3.

3.2. *Column Density: Constant Dust Emissivity*

Given the flux density at one wavelength and the dust temperature, the optical depth is given by:

$$\tau_\lambda = \frac{S_\lambda}{B_\lambda(T_d)} \tag{4}$$

where $B_\lambda(T_d)$ is the Planck function and S_λ is the observed flux density at wavelength λ.

The optical depth at wavelength λ can be converted to the V-band extinction (A_V) using the equation

$$A_V = X_\lambda \tau_\lambda \tag{5}$$

where X_λ is the scale factor, depending on the wavelength (λ) of the emission map, that relates the thermal emission properties of the dust grains to their V-band absorption properties (Eq. 5 from SRGL). We solve for X_λ for each pair of emission maps by minimizing the difference between the emission-derived column density (smoothed to the resolution of the extinction map) and the 2MASS absorption-derived column density, as in SRGL and SBG. For the 60/100 and 100/160 pair of emission maps we derive the optical depth and conversion factor (τ_{100} and X_{100}) from the 100 μm emission map. For the 70/160 pair of emission maps we derive τ_{160} and X_{160}, and scale both values in Figures 1 and 2 to the expected values at 100 μm assuming $\beta = 2$ using the scale factor $(\lambda_{100}/\lambda_{160})^\beta = 0.39$.

The optimization sets the overall calibration for the FIR data, but does not force the slope of NIR-derived column density plotted against FIR-derived column density to be exactly unity, though it will be close to this value. Variations in temperature along each line of sight will affect the emission-derived A_V at high column density more than at low column density, and the extinction-derived A_V is unaffected by temperature fluctuations. This difference in the way the dust temperature is coupled to the derived column density, along with possible variations in the FIR dust emissivity, can change the slope of the emission vs. absorption-derived column density to be slightly different from unity. Note that Eq. 5 assumes that the dust emission and absorption properties are constant. The linear relationship between τ_{FIR} and A_V is shown in Fig. 2.

3.3. *Column Density: Variable Dust Emissivity*

Just as the emission from VSG's is expected to vary with environment, so should the dust emissivity, due to such factors as grain growth through sticking and the formation of icy mantles. As a result of these processes, the dust emissivity in regions with higher column density and lower dust temperature is seen to be higher. This effect has been observed in many environments (e.g. Kiss et al. 2006; del Burgo & Laureijs 2005; Bernard et al. 1999), where it is shown that the FIR emissivity (α in Eq. 1 or X_λ in Eq. 5) anti-correlates with dust temperature and varies by a factor of a few in interstellar clouds similar to Perseus. In Fig. 2 we show the FIR dust emissivity (expressed as the ratio of the 100 μm optical depth and NIR-derived extinction) plotted against the color temperature of the dust. We also find this dependence of the emissivity on temperature and column density, which suggests that the linear fit between τ_{FIR} and A_V (see Eq. 5 and Fig. 2) does not fully describe the relationship between dust emission and absorption.

It is important to note that temperature fluctuations along the line of sight can give the appearance of a temperature-dependent emissivity when the dust is assumed to be isothermal, even if the true dust emissivity is constant. Because the line-of-sight averaged dust temperature is emission weighted, the dust temperature is overestimated and the far-infrared optical depth is underestimated. This effect is larger along lines of sight with greater temperature variation (i.e., those passing through denser regions), which are preferentially colder than the more diffuse (and nearly isothermal) portions of the molecular cloud. As a consequence, the derived ratio of the far-infrared optical depth to extinction will be underestimated in the colder, denser regions of the

molecular cloud. However, the observed temperature-dependent dust emissivity varies in the *opposite direction* of the correlation created by line-of-sight temperature fluctuations. The observed dust emissivity is *larger* at low temperatures, supporting the claim that the true dust emissivity is variable.

Noise in the FIR emission maps can also give the appearance of a variable dust emissivity. If noise changes the ratio of the fluxes, then the dust temperature will be either overestimated or underestimated. A high dust temperature will result in a low FIR-derived optical depth, and a low dust temperature will result in a high FIR optical depth. To illustrate the effect of noise on the derived dust emissivity, we analyze a simple model of a molecular cloud with constant dust emissivity in which the temperature is anti-correlated with column density and with both quantities are within a typical range for molecular clouds. We then derive the flux at 100 and 160 μm flux that would be emitted and add Gaussian random noise to the maps. We re-derive the dust temperature and 100 μm optical depth from the noisy maps and show the dust emissivity that would be estimated from the "observed" maps plotted against the temperature. The results are shown in Fig. 3. The dust emissivity that we derive in Perseus (see Fig. 4) looks similar to what one would expect from maps of dust that have a constant emissivity, but that have noise on the level of $\sim$15%. However, the random noise in all of our maps is much lower than this ($\lesssim$1%), so we can rule out the possibility that noise in the Perseus emission maps is tricking us into thinking that the dust emissivity is variable.

To account for the variable dust emissivity in the determination of the dust column density, we divide our data into the same ten equally populated bins as we did in Section 3.1, based on their NIR-derived extinction and temperature. Using Eq. 5, we derive the conversion (X_λ) separately for each bin and each pair of emission maps. The derived dust emissivity, as a function of T_d, is plotted in Fig. 1.

4. RESULTS

4.1. *VSG Emission and Dust Emissivity vs. T_d and A_V*

As shown in Fig. 1, the 60 and 70 μm emission is dominated by the emission from VSG's. The fractional contribution of BG emission rises with increasing T_d at both 60 and 70 μm. This is no surprise, given that warmer dust will have larger 60/100 and 70/160 μm flux ratios. At 70 μm, the BG contribution is a larger percentage of the total flux for $A_V > 2.6$ than $A_V < 2.6$, while at 60 μm the difference is smaller and changes sign. This difference may be caused by the 60 and 70 μm passbands, since IRAS is sensitive (sensitiviy $\geq$ 10%) from 37 to 82 μm while Spitzer is sensitive from 55 to 86 μm.

The parameter used to derive the dust column density from the FIR optical depth of the dust, as given by X_λ in Eq. 5, varies nearly identically with T_d for all three pairs of emission maps. The evolution in X_λ is primarily caused by the variable emissivity of the dust (shown in Fig. 2), but also by line-of-sight temperature fluctuations and noise in the emission maps. Taking into account variations in the VSG contribution to emission from dust with $\lambda < 100$ μm and variations in the emissivity of the BG's represents an increase in the complexity of the analysis performed in SRGL.

4.2. *Emission vs Absorption-derived Column Density*

As discussed in SRGL, the point to point scatter between emission and absorption-derived column density can be quite large (a few tens of percent). This scatter can be attributed to line-of-sight temperature fluctions, non-constant dust emissivity and variations in the fraction of emission coming from VSG's (though this last source of error should not affect the column density derived from emission maps at or above $\sim$100 μm).

In this paper we calculate the emission-derived column density in two ways. In the first method we assume that the dust emissivity is constant in Perseus, and that A_V scales with the FIR optical depth (Eq. 5). Our second method uses a dust emissivity which varies with A_V and T_d, as shown in Fig. 1. In both cases we correct for variations in the relative VSG/BG contribution to the 60 and 70 μm emission, as a function of T_d and A_V, as described in Section 3.1. The values for the median column density ratio, the scatter around that median, and the slope of the best fit line between the emission vs absorption-derived column density for Perseus are shown in Table 1 and the corresponding plots are shown in Fig. 4.

In SBG, we use a simplified model of emission from an externally heated molecular cloud to study the effects of line-of-sight temperature variations on column density estimates without having to worry about the effects of VSG emission or variations in the dust emissivity. Using that model, we predict that the scatter and bias should be largest for the 60/100 μm pair of maps and smallest for the 100/160 μm pair. However, in this paper, when we use a single $\tau - A_V$ conversion, we find that the slope and scatter between our emission and absorption-derived column densities are very similar for all three pairs of emission maps, in conflict with SBG. The amount of scatter in the NIR vs. 60/100 μm-derived column density is consistent with that predicted by the model in SBG. The larger than expected scatter seen in the 70/160 is probably not caused by an improper VSG correction, since we also find excess scatter in the NIR vs. 100/160 μm-derived column density, and VSG emission should be insignificant in the 100 and 160 μm maps.

When we divide the emission maps into ten subsets and derive the $\tau - A_V$ conversion for each bin (shown in Fig. 1), there is less bias in the emission-derived column density. This is shown by the fit between the FIR and NIR-derived column density in Fig. 4, which has a slope $\sim$1. However, the scatter in the relation (see Table 1) is only significantly improved for the 100/160 μm derived column density compared to the constant $\tau - A_V$ derivation. This suggests that the emission properties of dust are more complicated than assumed in this paper. For instance, the emissivity (or spectral index) of the dust could be density-dependent or there could be variations in grain properties as a function of position in Perseus, and not merely as a function of dust temperature and column density.

We conclude that the 100/160 μm pair of maps is the best for deriving dust temperature and column density because it is least affected by the emission from VSG's and has the least NIR vs. FIR column density scatter. However, since the 70/160 pair of emission maps has much better resolution, the column density and dust temperature maps produced from it are also useful if one

is willing to accept the additional uncertainty of using maps presented at $\sim 40''$ that have been calibrated on a $\sim 5'$ scale.

4.3. *Temperature and Column Density Maps*

Here we present dust temperature and column density maps derived from the IRAS and Spitzer fluxes. Figures 5, 6 and 7 show the temperature and column density maps derived from the IRAS and Spitzer far-infrared data and are presented at $\sim 5'$ resolution (which is the resolution of the NIR-derived extinction map and is approximately the resolution of the IRIS 60 and 100 μm maps). Figure 8 is derived from the Spitzer 70 and 160 μm data, and is presented at the $40''$ resolution of the 160 μm map (the 70 μm emission map was smoothed to the resolution of the 160 μm map). The column densities are determined by assuming a variable dust emissivity, as described in Section 3.3. Note that the VSG subtraction and variable dust emissivity are calibrated at $5'$ resolution, so the calibration of the dust temperature and column density using the Spitzer 70 and 160 μm maps present at $40''$ resolution is more uncertain than the maps presented at $5'$ resolution.

4.4. *Temperature and Column Density Histograms*

Figure 9 shows histograms of the dust temperature and column density distributions derived from from pairs of emission maps at 60/100, 70/160 and 100/160 μm. The 60 and 70 μm fluxes have been scaled to remove the VSG emission (as explained in Section 3.1). The median temperature derived for this region of the Perseus molecular cloud by Schlegel et al. (1998) is 16.5 K, whereas we derive a median temperature of 15.0 K, so our derived temperature is about 10% lower. The emission-derived column density is scaled to match that derived from the NIR reddening of background stars. Therefore, it is no surprise that the A_V distributions in all three panels of Fig. 9 are similar to that of the extinction map.

5. CONCLUSION

Using Spitzer 70 and 160 μm maps released by the c2d Legacy Project, we have created high-resolution dust temperature and column density maps of the Perseus molecular cloud. Although smaller in area than similar maps presented in SRGL using IRAS and 2MASS data, the maps in this paper (Fig. 7) are better calibrated to account for variations in the dust emissivity and removal of VSG emission. Combining the Spitzer 160 μm map with the IRAS 100 μm map we show that the dust temperature in Perseus is significantly colder (by $\sim$10%) than reported in the dust temperature map derived by Schlegel et al. (1998).

We find that the dust emissivity varies with A_V and T_d, in agreement with the results of del Burgo & Laureijs (2005) and Kiss et al. (2006). By fitting the absorption-derived column density to the FIR opacity in each of ten subsets of the data, we demonstrate an improved method for calculating the emission-derived dust column density. The column density derived from the 60/100 μm pair of emission maps, when compared with the NIR A_V, has slope and scatter consistent with those expected from variations in temperature along the line of sight. However, the scatter between the absorption-derived and 70/160 and 100/160 μm emission-derived column density is larger than would be expected from line-of-sight variations in the dust temperature alone. One possible explanation for the large scatter is that the 160 μm map is more sensitive to the emission from cold dust grains than are the 60 and 100 μm maps (SBG), and the dust emissivity varies more strongly at colder ($T_d < 15$ K) temperatures. Although the origin of the observed temperature dependence is uncertain, recent theoretical models of amorphous dust grains by Meny et al. (2007) and Boudet et al. (2005) also exhibit an anti-correlation between dust temperature and emissivity. Another possible cause for the higher dust emissivity at lower temperatures is that the dust grains could be accreting icy mantles in the dense and colder regions within the molecular cloud. Regardless of the reason, it is not surprising that dust grains with a higher emissivity, given their ability to cool more efficiently, will be found at lower equilibrium temperatures.

A temperature-dependent dust emissivity presents a challenge for those attempting to derive dust temperatures and column densities from FIR emission maps. In SBG, we suggest that longer-wavelength ($\lambda > 100$ μm) emission maps should be used to calculate the line-of-sight dust properties because of their decreased sensitivity to fluctuations in the dust temperature and the lack of confusing emission from VSG's. In this paper, we show that the dust emissivity anti-correlates with dust temperature, and that the variability is likely to increase at lower temperatures, an effect which is also seen in other regions (e.g., del Burgo & Laureijs 2005; Kiss et al. 2006). This complicates the interpretation of longer wavelength emission maps, which are more sensitive to cold dust. The deleterious effects of VSG emission, temperature gradients, and variable dust emission properties add complexity to the determination of the mass and temperature distributions of dust in a molecular cloud. Resolution of these problems may require coverage from tens to hundreds of microns, finer spectral resolution than the broad IRAS and Spitzer filters provide, and comparison with dust emission models of "realistic" molecular clouds.

Given the complexity of determining column density from dust emission, one may wonder if using extinction might be a superior method. For instance, the extinction map of Perseus made with 2MASS data and the NICER algorithm (Ridge et al. 2006; Lombardi & Alves 2001) is used as a template with which we calibrate the emission-derived column density in this paper, and we trust extinction-derived column density more than that derived from dust emission in general (Goodman et al. 2008; Pineda et al. 2008). The resolution of extinction maps is limited by the number of background tracers with known color, which provide $1'$ resolution for clouds nearby the galactic center in projection (Lombardi et al. 2006), but is coarser towards clouds further away from the galactic plane. However, emission maps are limited only by the size of the detector and also provide information on the dust temperature.

We would like to thank our anonymous referee for substantially improving the scope and clarity of this paper. Scott Schnee acknowledges support from the Owens Valley Radio Observatory, which is supported

by the National Science Foundation through grant AST 05-40399. Alyssa Goodman acknowledges support from the National Science Foundation under Grant No. AST-0407172.

REFERENCES

Bernard, J. P., et al. 1999, A&A, 347, 640
Bethell, T. J., Zweibel, E. G., Heitsch, F., & Mathis, J. S. 2004, ApJ, 610, 801
Boudet, N., Mutschke, H., Nayral, C., Jäger, C., Bernard, J.-P., Henning, T., & Meny, C. 2005, ApJ, 633, 272
Boulanger, F., Falgarone, E., Puget, J. L., & Helou, G. 1990, ApJ, 364, 136
del Burgo, C., & Laureijs, R. J. 2005, MNRAS, 360, 901
Draine, B. T., & Lee, H. M. 1984, ApJ, 285, 89
Draine, B. T., & Li, A. 2001, ApJ, 551, 807
Evans, N. J., II, et al. 2003, PASP, 115, 965
Goodman, A. A., Pineda, J. & Schnee, S. ApJ, in prep.
Gordon, K. D., et al. 2007, PASP, 119, 1019
Heitsch, F., Zweibel, E. G., Mac Low, M.-M., Li, P., & Norman, M. L. 2001, ApJ, 561, 800
Kiss, C., Ábrahám, P., Laureijs, R. J., Moór, A., & Birkmann, S. M. 2006, MNRAS, 373, 1213
Laureijs, R. J., Chlewicki, G., Wesselius, P. R., & Clark, F. O. 1989, A&A, 220, 226
Laureijs, R. J., Clark, F. O., & Prusti, T. 1991, ApJ, 372, 185
Li, A., & Draine, B. T. 2001, ApJ, 554, 778
Lombardi, M., Alves, J., & Lada, C. J. 2006, A&A, 454, 781
Lombardi, M., & Alves, J. 2001, A&A, 377, 1023
Mathis, J. S., Rumpl, W., & Nordsieck, K. H. 1977, ApJ, 217, 425
Mathis, J. S., Mezger, P. G., & Panagia, N. 1983, A&A, 128, 212
Meny, C., Gromov, V., Boudet, N., Bernard, J. -., Paradis, D., & Nayral, C. 2007, ArXiv Astrophysics e-prints, arXiv:astro-ph/0701226
Miville-Deschênes, M.-A., & Lagache, G. 2005, ApJS, 157, 302
Pineda, J. E., Caselli, P., & Goodman, A. A. 2008, ArXiv e-prints, 802, arXiv:0802.0708
Rebull, L. M., et al. 2007, ApJS, 171, 447
Ridge, N. A., et al. 2006, AJ, 131, 2921
Schlegel, D. J., Finkbeiner, D. P., & Davis, M. 1998, ApJ, 500, 525
Schnee, S., Kauffmann, J., Goodman, A., & Bertoldi, F. 2007, ApJ, 657, 838
Schnee, S., Bethell, T., & Goodman, A. 2006, ApJ, 640, L47
Schnee, S. L., Ridge, N. A., Goodman, A. A., & Li, J. G. 2005, ApJ, 634, 442
Stansberry, J. A., et al. 2007, PASP, 119, 1038
Stepnik, B., et al. 2003, A&A, 398, 551
Wood, D. O. S., Myers, P. C., & Daugherty, D. A. 1994, ApJS, 95, 457

TABLE 1
Emission vs. Absorption-Derived Column Density

Emission Maps	μ^a constant	μ^b variable	σ^c constant	σ^d variable	slope^e constant	slope^f variable
60/100 μm	1.01	1.00	0.32	0.31	0.80	0.88
70/160 μm	1.00	1.00	0.34	0.32	0.90	1.03
100/160 μm	1.00	1.00	0.30	0.25	0.77	0.91

[a] Median ratio of $A_{V,emission}/A_{V,extinction}$ assuming a constant dust emissivity
[b] Median ratio of $A_{V,emission}/A_{V,extinction}$ assuming a variable dust emissivity
[c] 1 σ scatter in $A_{V,emission}/A_{V,extinction}$ assuming a constant dust emissivity
[d] 1 σ scatter in $A_{V,emission}/A_{V,extinction}$ assuming a variable dust emissivity
[e] Best fit slope from Figure 4 (left)
[f] Best fit slope from Figure 4 (right)

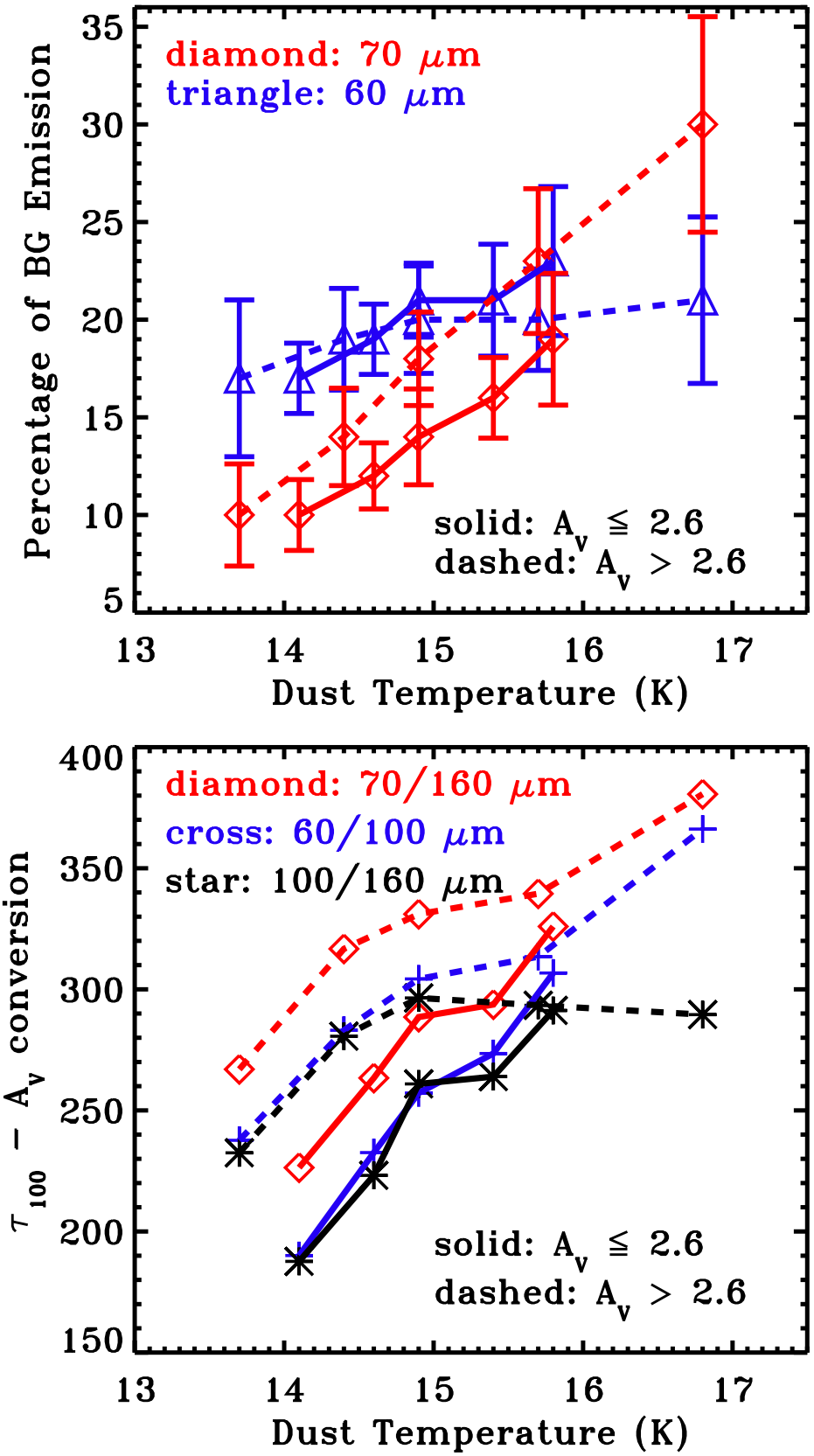

FIG. 1.— (*top*) The percentage of the observed 60 and 70 μm flux emitted by BG's in thermal equilibrium as a function of dust temperature. The remaining portion is emitted by stochastically heated VSG's. The error bars show the standard deviation in each bin. (*bottom*) The ratio of the observed extinction to the 100 μm optical depth as a function of dust temperature. For the 70/160 μm pair of emission maps, we derive τ_{100} assuming that $\beta = 2$ and scaling τ_{160} by $(100/160)^{\beta}$. In both the top and bottom plots there are 151 ± 15 independent $5'$ data values in each bin.

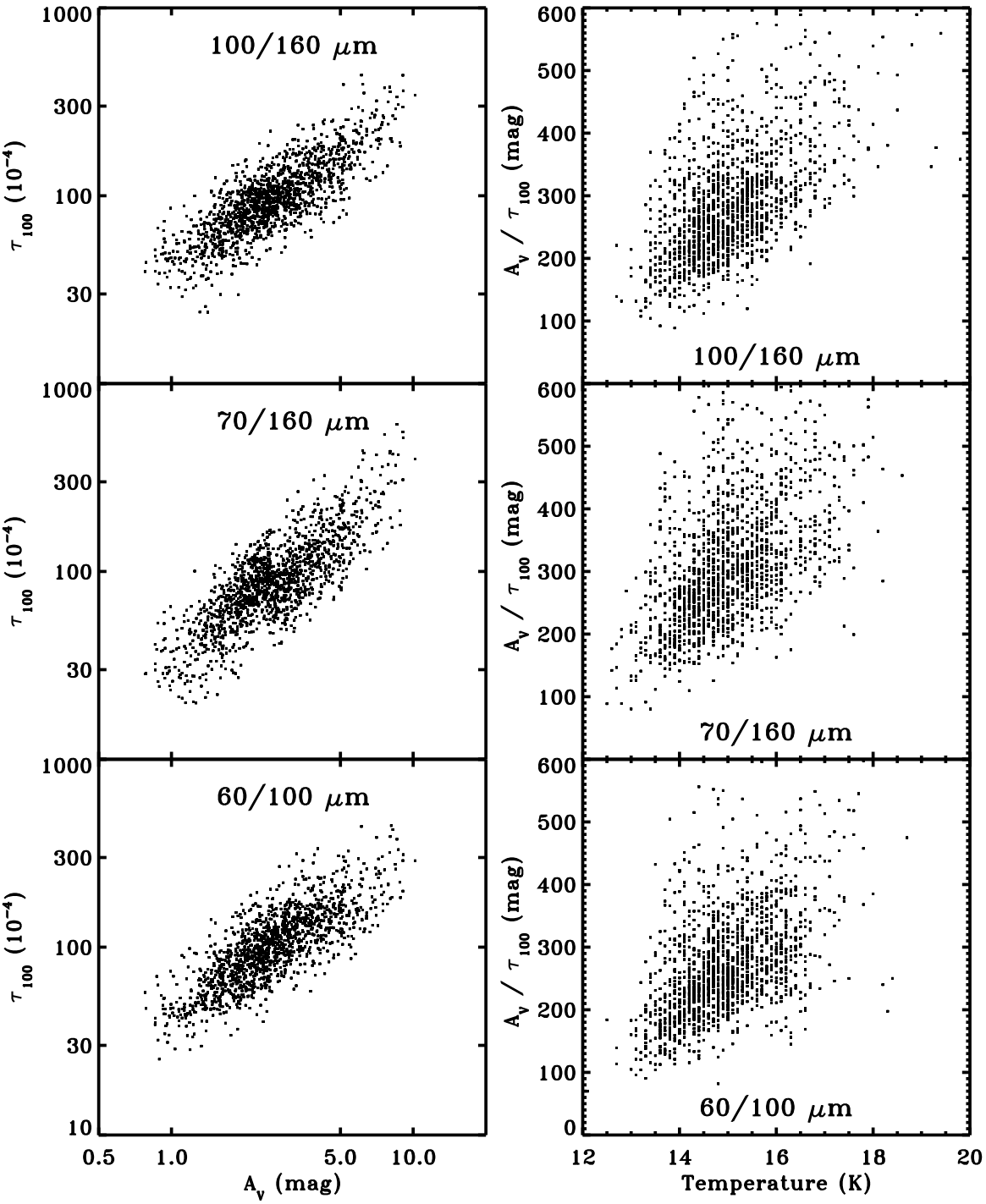

FIG. 2.— (*left*) The 100 μm optical depth plotted against the column density (expressed in terms of V-band extinction) derived from the 2MASS map. (*right*) The ratio of the NIR-derived column density divided by the FIR-derived optical depth (at 100 μm) plotted against the FIR-derived dust temperature.

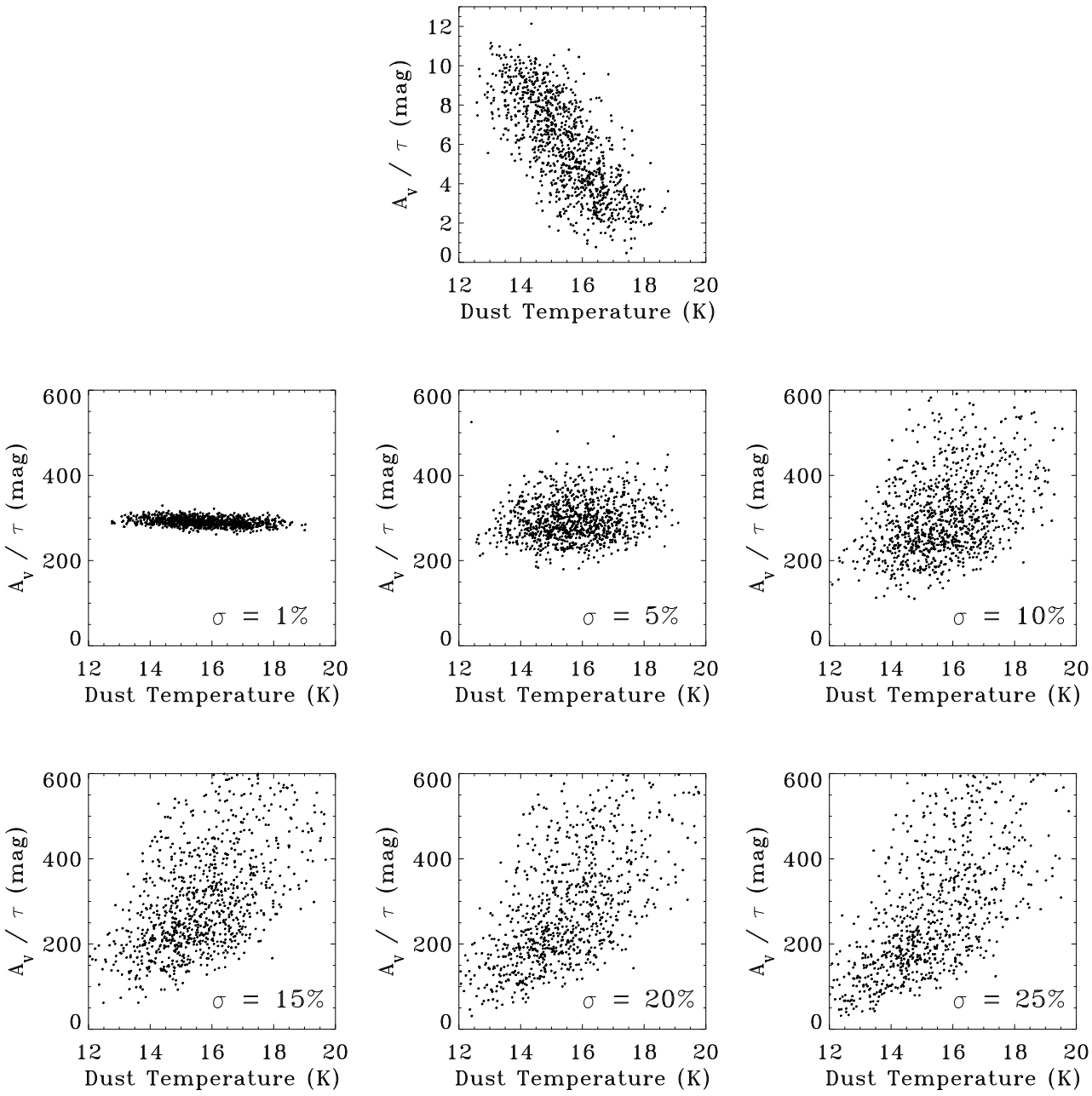

FIG. 3.— (*Top*) A model temperature and column density distribution, which will be used to generate synthetic emission maps and test the effects of noise on the derived dust emissivity. (*Middle and Bottom*) The dust emissivity, expressed as the ratio of the 100 μm optical depth and the column density, plotted against dust temperature. The optical depth and dust temperature are derived from synethic flux maps at 100 and 160 μm, with relative noise levels ranging from 1% to 25%. The "true" flux is calculated from the column density and temperature distibution in the top panel, and is then adjusted by Gaussian random noise at the level shown in each middle and lower panel.

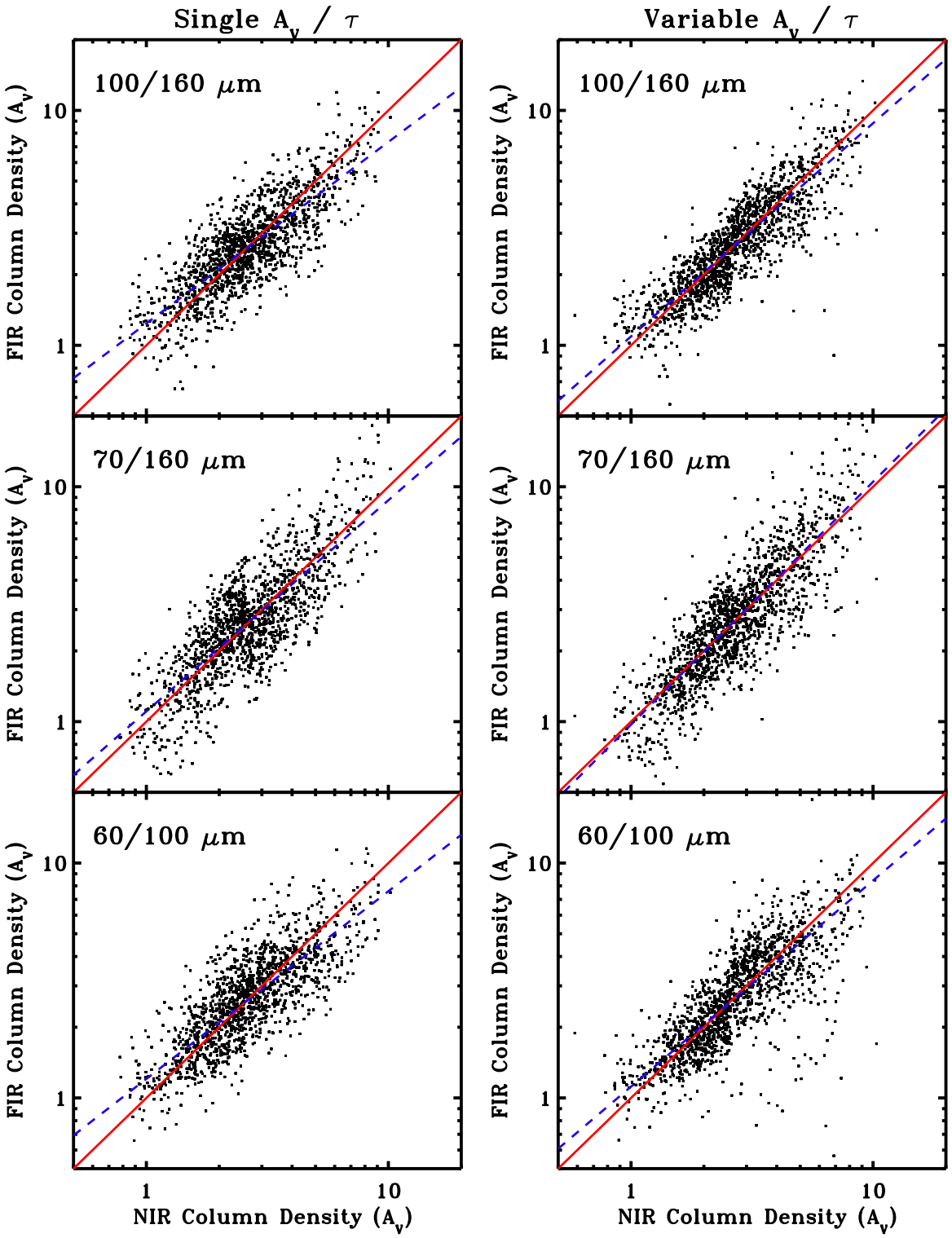

FIG. 4.— (*left*) The FIR-derived column density plotted against the NIR-derived column density. Here we assume a single value for the dust emissivity for each pair of emission maps. (*right*) The FIR-derived column density plotted against the NIR-derived column density. Here we assume a variable value for the dust emissivity for each pair of emission maps, as plotted in Fig. 1.

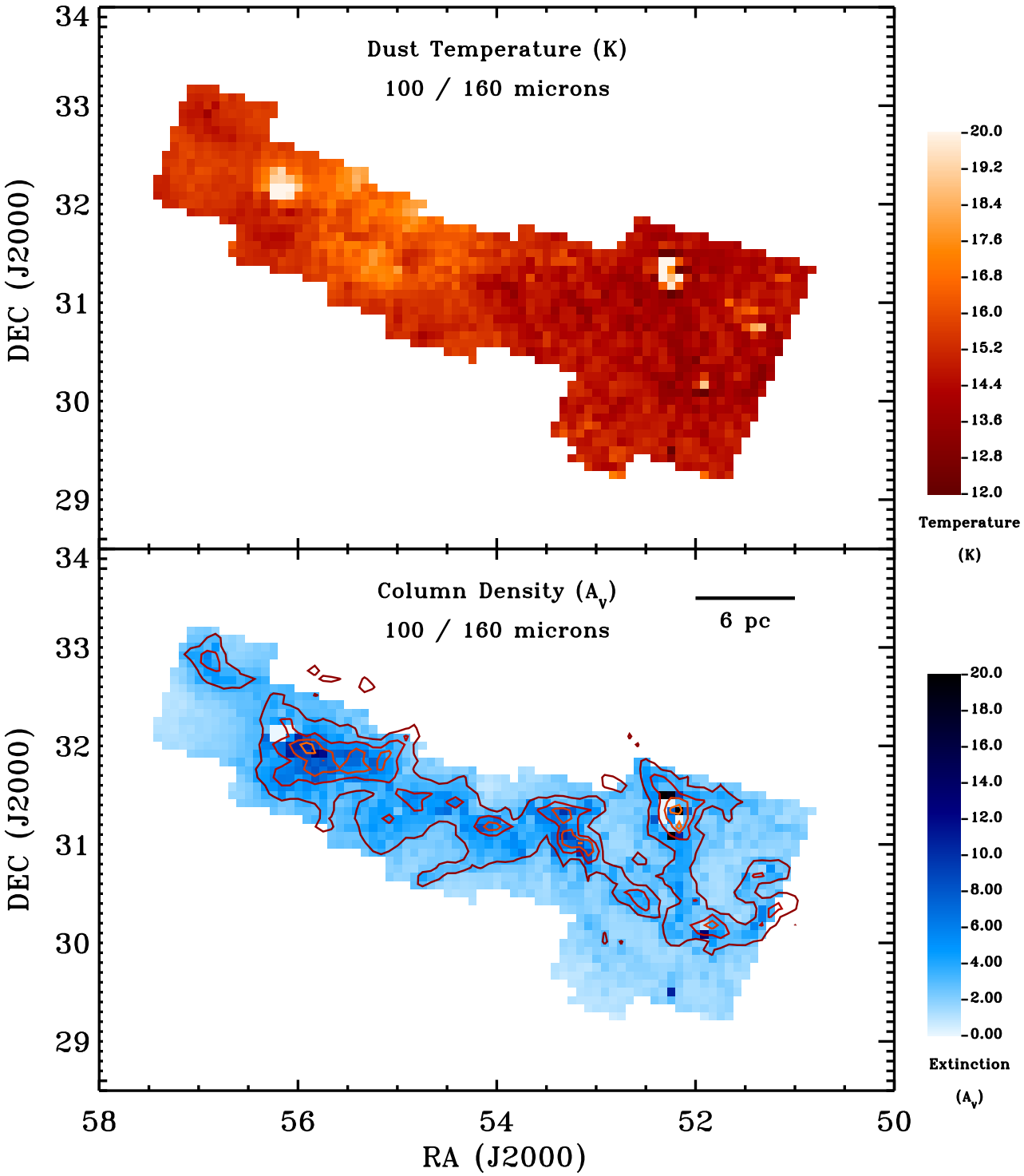

FIG. 5.— (*top*) The dust temperature map and (*bottom*) column density (expressed in terms of V-band extinction) derived from the IRAS 100 and Spitzer 160 μm flux density maps, at the 5′ resolution of our NIR-derived extinction map. The column density is derived assuming a variable dust emissivity. Red contours in the bottom plot show the regions with extinction of $A_V = 3, 5, 7, 9$.

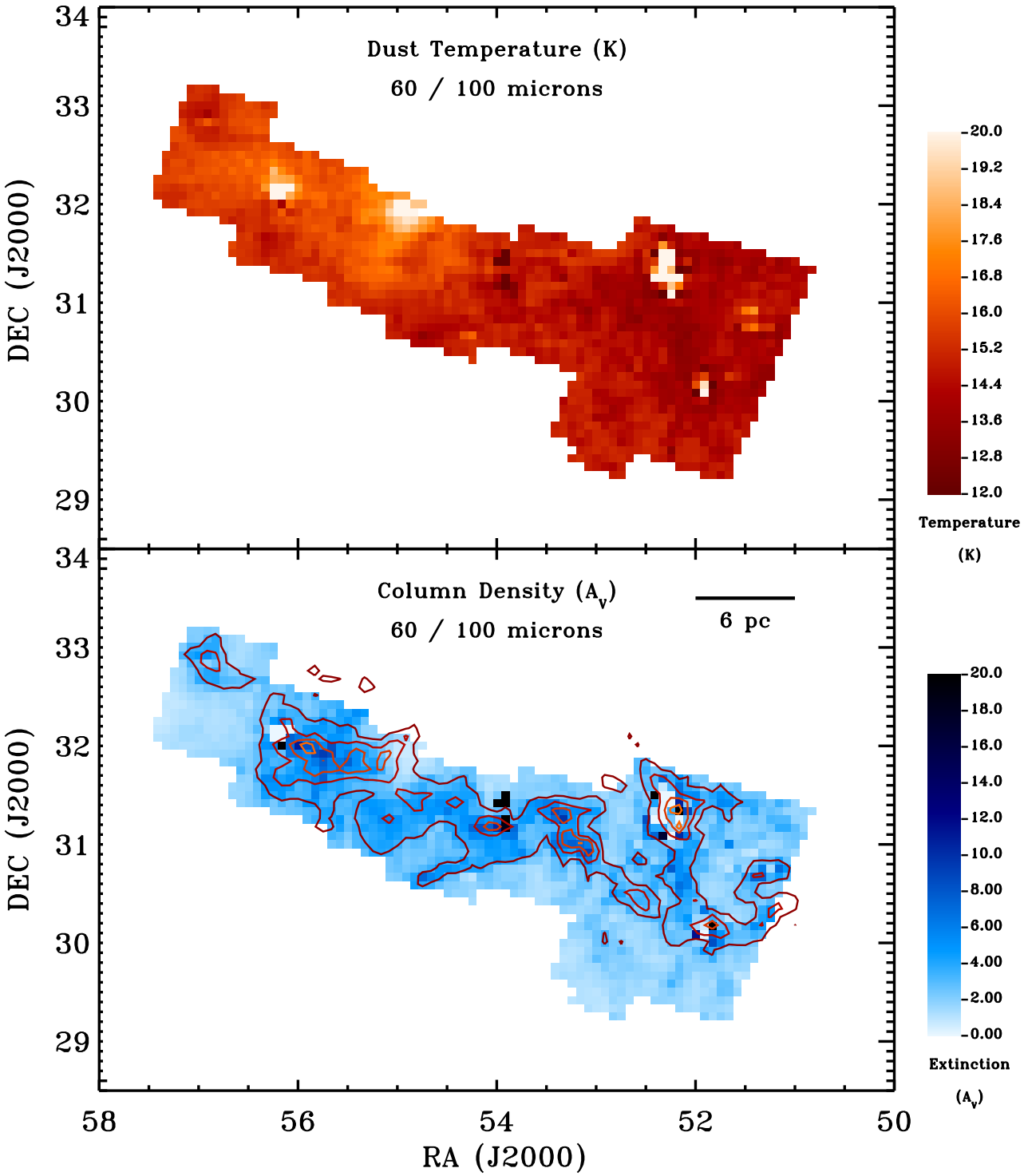

FIG. 6.— (*top*) The dust temperature map and (*bottom*) column density (expressed in terms of V-band extinction) derived from the IRAS 60 and 100 μm flux density maps, at the 5′ resolution of our NIR-derived extinction map. The column density is derived assuming a variable dust emissivity. Red contours in the bottom plot show the regions with extinction of $A_V = 3, 5, 7, 9$.

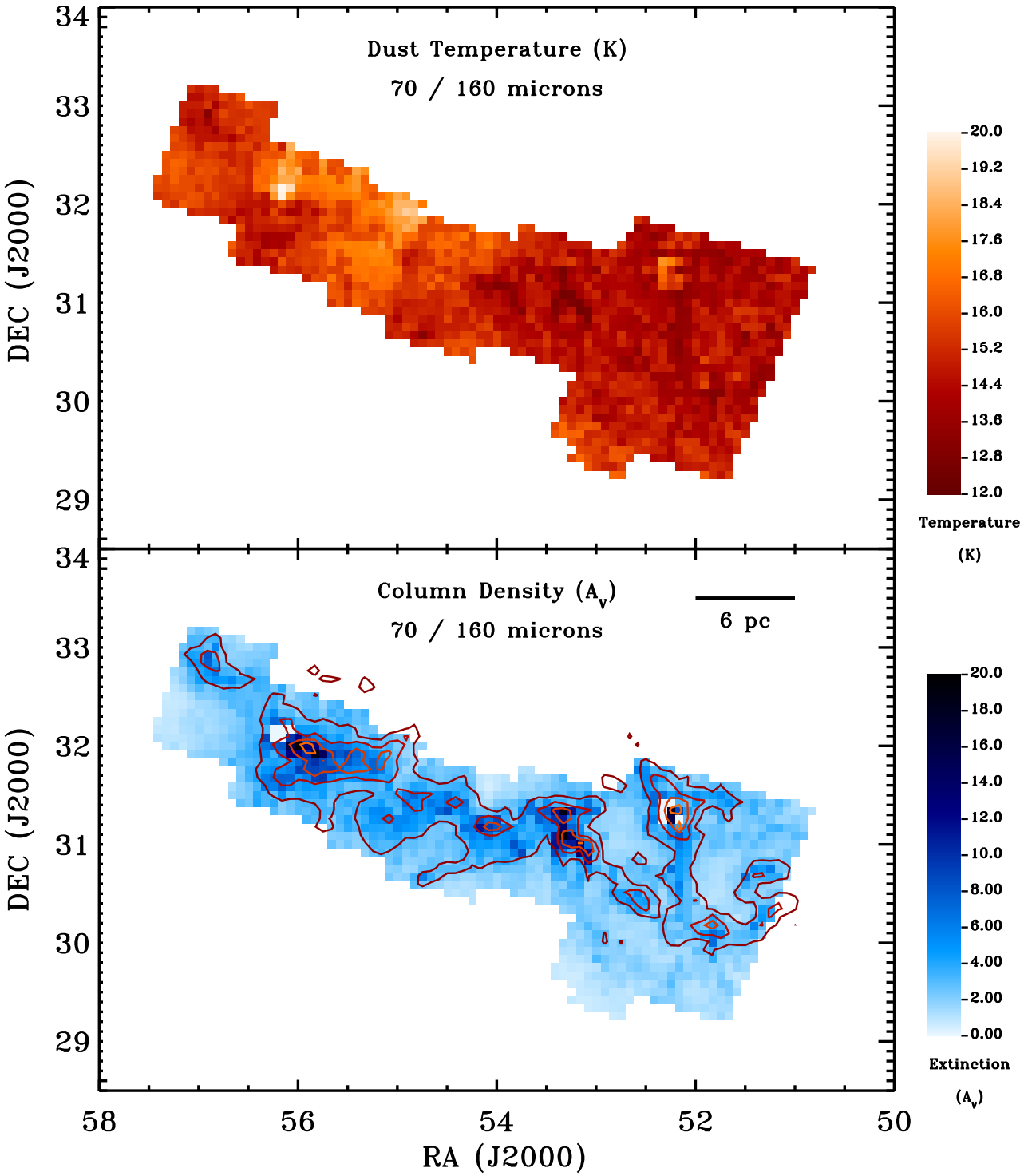

FIG. 7.— (*top*) The dust temperature map and (*bottom*) column density (expressed in terms of V-band extinction) derived from the Spitzer 70 and 160 μm flux density maps, at the 5′ resolution of our NIR-derived extinction map. The column density is derived assuming a variable dust emissivity. Red contours in the bottom plot show the regions with extinction of $A_V = 3, 5, 7, 9$.

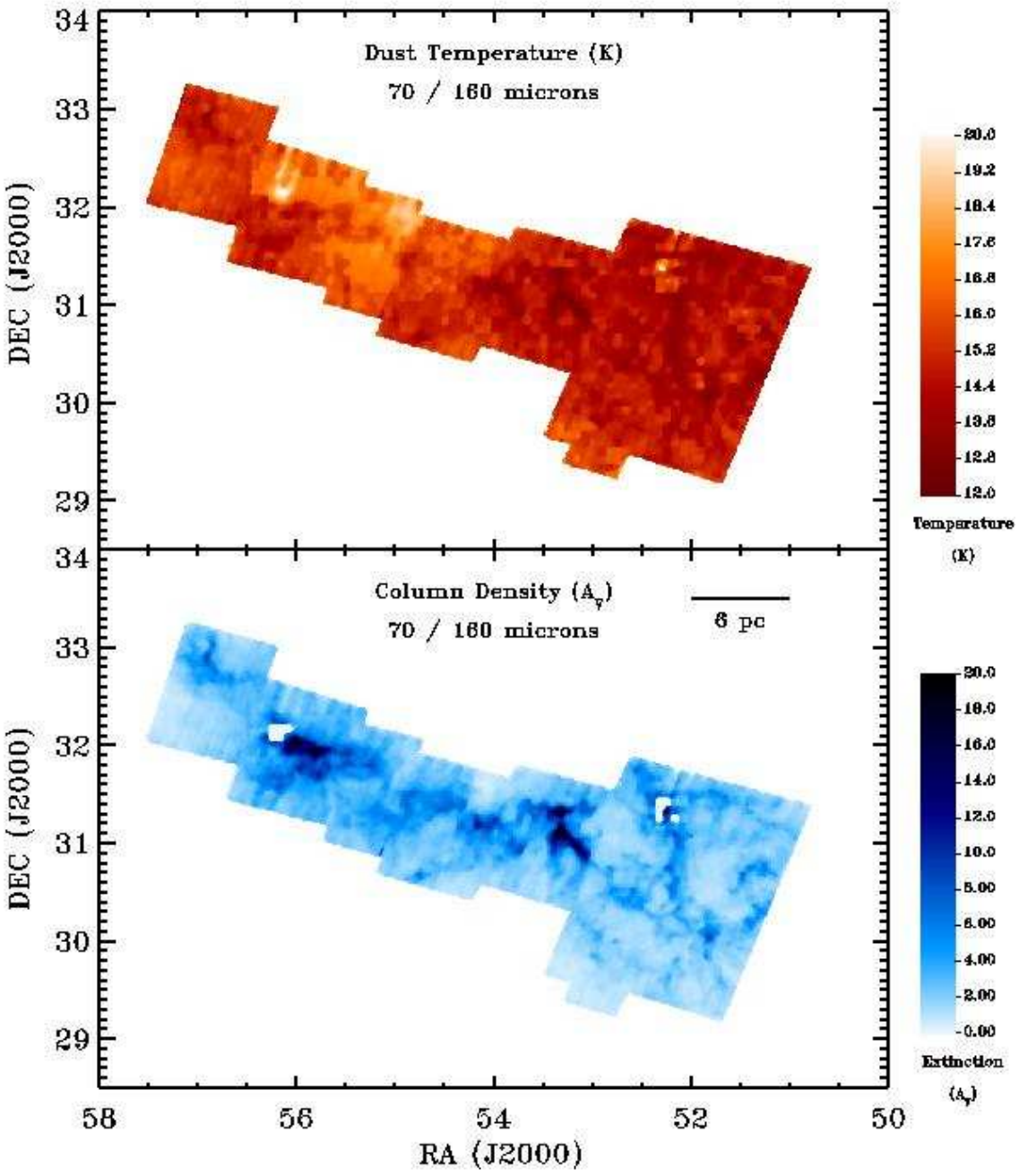

FIG. 8.— (*top*) The dust temperature map and (*bottom*) column density (expressed in terms of V-band extinction) derived from the Spitzer 70 and 160 μm flux density maps, at the $40''$ resolution of the 160 μm map. The column density is derived assuming a variable dust emissivity. Red contours in the bottom plot show the regions with extinction of $A_V = 3, 5, 7, 9$.

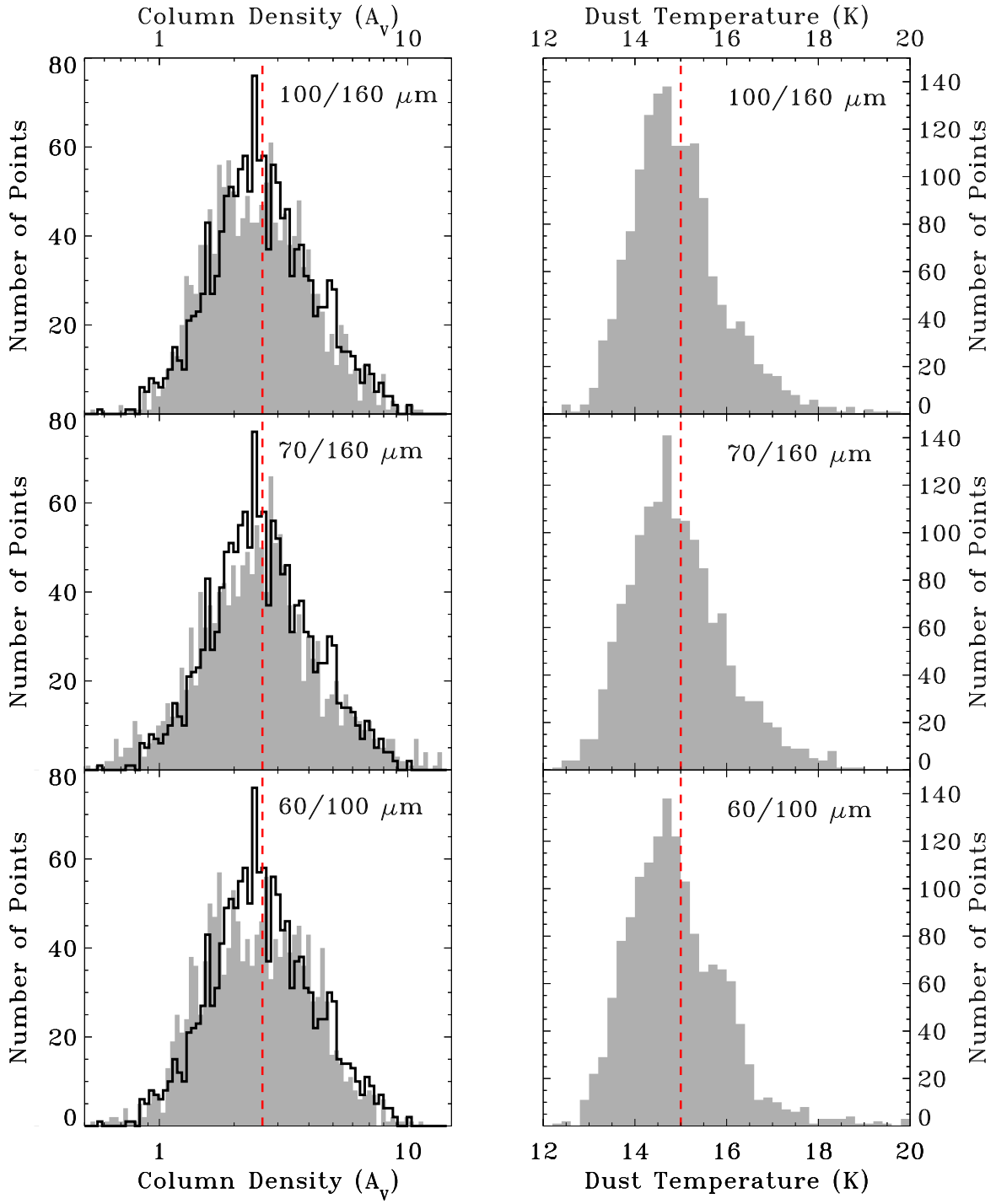

FIG. 9.— Histograms of the dust color temperature and column density derived from the IRAS 60 and IRAS 100 μm flux density maps (*bottom*), Spitzer 70 and 160 μm flux density maps (*middle*) and IRAS 100 and Spitzer 160 μm flux density maps (*top*). The column density is derived assuming a variable dust emissivity. The dust temperature is derived assuming a variable fraction of 60 and 70 μm flux emitted by BG's. The filled histograms show the column density and temperature derived from FIR emission, while the open histograms show the column density derived from NIR absorption. The vertical dashed lines show the median A_V in the 2MASS map (*left*) and the median dust temperature in the 100/160 μm T_d map (*right*).